Biosensors and Bioelectronics 138 (2019) 111284

Contents lists available at ScienceDirect

Biosensors and Bioelectronics

journal homepage: www.elsevier.com/locate/bios

MyoRobot 2.0: An advanced biomechatronics platform for automated, environmentally controlled skeletal muscle single fiber biomechanics assessment employing inbuilt real-time optical imaging

M. Haug[a,1], C. Meyer[a,1], B. Reischl[a], G. Prölß[a], S. Nübler[a], S. Schürmann[a], D. Schneidereit[a], M. Heckel[b], T. Pöschel[b], S.J. Rupitsch[c], O. Friedrich[a,d,e,*]

[a] *Institute of Medical Biotechnology, Friedrich-Alexander-University Erlangen-Nürnberg, Paul-Gordan-Str. 3, 91052, Erlangen, Germany*
[b] *Institute of Multi Scale Simulation of Particulate Systems, Friedrich-Alexander-University Erlangen-Nürnberg, Nägelsbachstrae 49b, 91052, Erlangen, Germany*
[c] *Institute of Sensor Technology, Friedrich-Alexander-University Erlangen-Nürnberg, Paul-Gordan-Str. 3/5, 91052, Erlangen, Germany*
[d] *School of Medical Sciences, Faculty of Medicine, University of New South Wales, Wallace Wurth Building, 18 High St, Kensington, NSW, 2052, Australia*
[e] *Muscle Research Center Erlangen (MURCE), Erlangen, Germany*

ARTICLE INFO

Keywords:
MyoRobot
Skeletal muscle
EDL
Single fiber
Sarcomere length
Temperature control
Biosensor
Biomechatronics
Ca^{2+} sensitivity
Axial compliance
Young's modulus

ABSTRACT

We present an enhanced version of our previously engineered *MyoRobot* system for reliable, versatile and automated investigations of skeletal muscle or linear polymer material (bio)mechanics. That previous version already replaced strenuous manual protocols to characterize muscle biomechanics properties and offered automated data analysis. Here, the system was further improved for precise control over experimental temperature and muscle single fiber sarcomere length. Moreover, it also now features the calculation of fiber cross-sectional area via *on-the-fly* optical diameter measurements using custom-engineered microscope optics. With this optical systems integration, the *MyoRobot 2.0* allows to tailor a wealth of recordings for relevant physiological parameters to be sequentially executed in living single myofibers. Research questions include assessing temperature-dependent performance of active or passive biomechanics, or automated control over length-tension or length-velocity relations. The automatically obtained passive stress-strain relationships and elasticity modules are important parameters in (bio)material science. From the plethora of possible applications, we validated the improved *MyoRobot 2*.0 by assessing temperature-dependent myofibrillar Ca^{2+} sensitivity, passive axial compliance and Young's modulus. We report a Ca^{2+} desensitization and a narrowed dynamic range at higher temperatures in murine *M. extensor digitorum longus* single fibers. In addition, an increased axial mechanical compliance in single muscle fibers with Young's moduli between 40 - 60 kPa was found, compatible with reported physiological ranges. These applications demonstrate the robustness of our *MyoRobot 2.0* for facilitated single muscle fiber biomechanics assessment.

1. Introduction

Motility is an essential pre-requisite for life in the animal kingdom. In fact, skeletal muscle is the main organ transducing electrical nerve signals into contractile activity of motor protein complexes. This process is called excitation-contraction coupling (Ebashi, 1976; Berchtold et al., 2000) and involves chemical Ca^{2+} signalling. Malfunctions within the electro-chemical cascade of protein biopolymer activation at the interface of actin and myosin filaments mostly result in loss-of-function symptoms of muscle weakness and impaired mobility. Although muscle research has been and still is a vital area in physiology and neurology, the discovery of numerous genetic mutations in genes involving muscle regulation could not be matched by the increased demand for functionality studies. Reasons are tedious research protocols to assess the biomechanics of whole muscle, small fiber bundles or even single fibers (Lamb and Stephenson, 2018). There is a tremendous need for highly automated and throughput-increasing technologies in myology. Such multidisciplinary challenges could potentially open up

---

* Corresponding author. Institute of Medical Biotechnology, Friedrich-Alexander-University Erlangen-Nürnberg, Paul-Gordan-Str. 3, 91052, Erlangen, Germany.
E-mail addresses: michael.haug@fau.de (M. Haug), charlotte.pollmann@fau.de (C. Meyer), barbara.reischl@fau.de (B. Reischl), ger.proelss@fau.de (G. Prölß), stefanie.diermeier@fau.de (S. Nübler), sebastian.schuermann@fau.de (S. Schürmann), dominik.schneidereit@fau.de (D. Schneidereit), michael.heckel@fau.de (M. Heckel), thorsten.poeschel@fau.de (T. Pöschel), stefan.rupitsch@fau.de (S.J. Rupitsch), oliver.friedrich@fau.de (O. Friedrich).

[1] These authors contributed equally.

https://doi.org/10.1016/j.bios.2019.04.052
Received 25 March 2019; Accepted 24 April 2019

new possibilities in emerging fields, e.g. personalized medicine, organ printing or tissue engineering and biomedical engineering. These disciplines require extensive studies, as close to physiological conditions as possible. Thus, development and implementation of new technologies to facilitate expanding our knowledge of muscle biomechanics (Head, 2010; Friedrich et al., 2014) and (bio)materials are a promising biomedical engineering mission. We recently introduced the *MyoRobot* automated biomechatronics system as a multi-purpose platform that meets the requirements of high experimentation numbers, repeatability through automated recordings and stability and reproducibility of results through objective algorithm analysis (Haug et al., 2018). Apart from its range of application, not being limited to muscle research only, the *MyoRobot* has proven very effective for investigating active and passive biomechanics properties of muscle fibers combining state-of-the-art force transducer (FT) sensor, stepper motor and voice coil (VC) actuator technologies.

Still, major limitations of the system were that (i) an environmental temperature control, desired by many physiologists to establish Q10 values to derive functional kinetics parameters, and (ii) an in-built optical metrology to automatically monitor single fiber diameter and sarcomere length (SL) patterns, were not yet available. The latter would allow to directly normalize forces to cross-sectional area (so-called specific force) and to precisely adjust SL to define global starting points for resting length-tension curves across individual fibers. This would eliminate large scattering of recorded active forces, typically arising from individual fiber calibre variability within a muscle and allow a better comparison with literature values, usually given in N/mm^2 or kPa (Lännergren and Westerblad, 1987; Sam et al., 2000; Mendias et al., 2011). Furthermore, it would also eliminate different degrees of slack of fibers in stress-strain relationships due to starting at defined SLs rather than absolute fiber resting lengths L_0 (Haug et al., 2018). Thus, we here improved our *MyoRobot* system to enable user control over these parameters. The first improvement consists of a heated metal alloy multi-well rack which came along with the necessity to install stronger and faster linear actuation motors and integrating water bath fluid connectors for liquid heating into the rack's wall. Turbulence chambers inside the walls minimized heating time and ensured steady temperature control over time. Moreover, the rack's glass bottom allows constant visual feedback of the specimen via the in-built microscope optics. The optics provide a magnification of approx. 24 x. This enables the live determination of fiber diameter and SL, prior to or during any recordings, using our custom-written *MyoRobot 2.0* GUI, called *MyoWizard*. These improvements, presented in Fig. 1, substantially increase the versatility of the *MyoRobot* and predispose this device for automated higher throughput modern biomechanics research in myology and biomaterials.

2. Results

2.1. The thermo-controlled rack: stable temperature profiles and homogeneous heat distribution

Compensation for possible heat loss along connecting hoses and latency between set and measured water bath temperature was assessed in calibration experiments before recording any muscle samples. Water bath temperature was additionally monitored by two external sensor at well #15 and #1. Fig. 2 displays the calibration curves, measured within the water bath and heated rack, for physiological limb temperature (32 °C (Bigland and Zaimis, 1958), Fig. 2A) and core body conditions (37 °C, Fig. 2B). Both calibration curves yield a heating progression of $\frac{1^{o}C}{5min}$ and confirm an offset of 1 °C between set and measured water bath temperature, and another 1 °C loss compared to the actual rack temperature. Applying slightly higher temperatures (+2 °C), rack temperature was constantly held at 32 °C or 37 °C over 300 min. Moreover, temperature profiles displayed no major differences between external and internal heat sensors, even at distant rack position numbers, i.e. #15 or #1. This confirms an effective insulation and heat distribution for the chosen materials, rack design and in-built turbulence chambers.

2.2. Increased evaporation and augmented osmolality after 2 h of recording above room temperature

Due to the high sensitivity of the troponin-C Ca^{2+} biosensor in the micromolar range and its strong dependence on environmental factors, even minimal changes in ionic strength, pH and osmolality may lead to a biased experiment outcome. Therefore, we quantitated changes to the bath solution compositions by conducting an evaporation assay. This included increasing temperatures to determine the maximum recording time during which osmolality changes remained within a minimum acceptable range (±5%, i.e. ~2 hrs; Fig. 3). Observations showed that evaporation was neglectable at room temperature (RT, 22 °C) within an extended recording interval per muscle preparation. At RT, neither a weight loss of the basin volume, nor consequent osmolality alterations were detected within 2 h. In our experience from past studies using the previous *MyoRobot* system at RT, we did not expect changes even for longer durations (up to 6 h). Subsequently, rack temperature was increased to 32 °C, causing a basin solution weight loss of approx. 2.5 % w/h and a parallel increase in osmolality of approx. 3.75%/h. Ultimately, these observations suggest keeping recording time at temperatures above RT below 2 h to avoid osmolality changes greater than 5%, and to minimize solution evaporation.

2.3. Automated MyoRobot 2.0 recordings of myofibrillar Ca^{2+} biosensor sensitivity at different (physiological) temperatures

Initial tests with the *MyoRobot 2.0* heated rack involved temperature dependent assessment of maximum isometric force and troponin-C Ca^{2+} sensitivity in the same single fiber. While absolute force in single fibers only was ~0.1 mN at RT, an increase to 32 °C or 37 °C yielded an over two-fold augmented F_{max} and thus, improved performance (Fig. 4A). This enhancement with temperature is likewise reflected in the caffeine-induced SR Ca^{2+} release force transients (F_{caff}), whose maximum amplitude reveals an over three-fold increase under heated conditions. Apparently, fibers at limb temperature (32 °C) perform better than their RT counterparts and further imply a slight amplitude increase compared to 37 °C, which is also reflected in the ratio of $F_{caff,peak}/F_{max}$.

Addressing the calcium sensitivity in pCa-force experiments (Fig. 4B, top row) reveals a right-shift and increase in curve steepness at higher temperatures. Indeed, group analysis (Fig. 4B) suggests a two-fold larger Hill-coefficient for fibers at 37 °C over those recorded at RT. This points towards a decreased dynamic range due to an increased stoichiometric number of Ca^{2+} binding sites at the myofibrillar interface of troponin-C, although this was not statistically significant. On the contrary, the pCa_{50} value appears to decrease steadily under warmer, more physiological conditions, indicative of a calcium desensitization compared to experiments carried out at RT.

2.4. Camera calibration confirms μm-resolution of the engineered optics

A major improvement of our *MyoRobot 2.0* system was implemented as an in-built optics to visualize single fibers during biomechanical recordings without the requirement of external research microscopes. Results on camera calibration and resolution can be found in the SI.

2.5. Benchmarking of MyoRobot 2.0 fiber cross section and sarcomere length analysis on-the-fly against subsequent multiphoton SHG imaging

Before applying the *MyoRobot 2.0*, the system was benchmarked against SHG images of the same fiber. Further information on *MyoRobot*

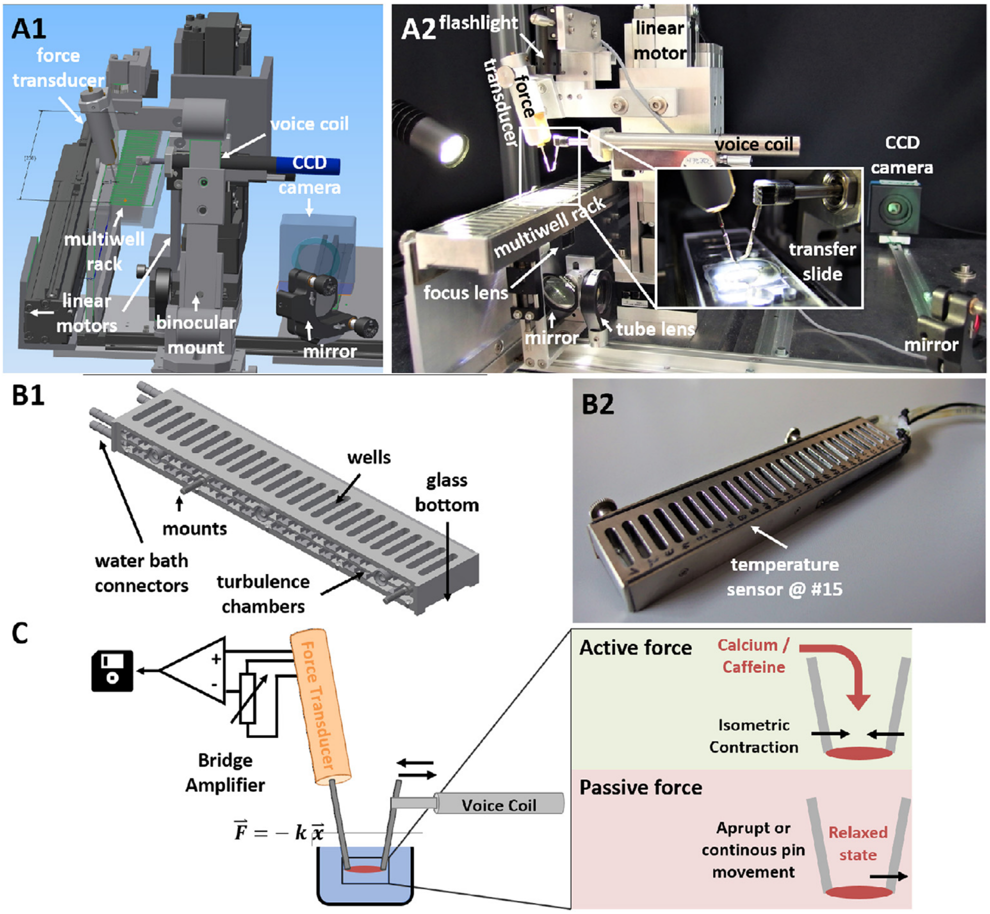

Fig. 1. CAD design and photographs of the *MyoRobot 2.0* with in-built engineered optics and temperature-controlled linear rack.A1 & A2, CAD model and picture of the assembled *MyoRobot 2.0* shown in side-view perspective, including markers for important components. The white box shows the transfer slide used for fiber mounting **B1**, displays the CAD design model of the heated rack featuring water bath connectors for external heating and turbulence chambers promoting homogeneous fluidics and coolant distribution. The wells are sealed with a glass bottom enabling optical access to the mounted sample. **B2**, presents a photograph of the assembled rack and fluid connectors. A temperature sensor was built into well #15. **C**, the FT-VC arrangement uses Hooke's law to record exerted forces. Active force is triggered by exposing the preparation to Ca^{2+}- or caffeine-containing solution. Passive force is assessed by stretching the (relaxed) preparation. The output signal is passed through a bridge amplifier, digitized and saved to a computer.

2.0 benchmarking can be found in the SI.

Fig. 5 presents a single EDL fiber imaged with *MyoRobot 2.0* optics and processed with the implemented algorithm to assess (i) fiber cross section, indicated by the red edges fitted to the yellow dots and (ii) SL, determined along the green line running across the fiber. The line profile (Fig. 5B) was processed using two different techniques, *rising edge* of derivative (left panel) and *FFT* of derivative (right panel), to provide two independent measures for sarcomere spacing. Both methods calculated SL to ~2.5 μm, which agrees well with the average SL obtained by image analysis of 3D SHG stacks from the same fiber following *MyoRobot* experiments (Fig. 5C), computing a value of 2.56 μm. A cross-validation from five single fibers (Table 1, SI) confirms the robustness of the implemented detection algorithm by matching SLs computed with the *MyoRobot 2.0* compared to SHG analysis. There was no statistical difference between SHG and average *MyoWizard* results. This concludes the reliable application of the *MyoRobot 2.0* software for *on-the-fly* sarcomere measurements.

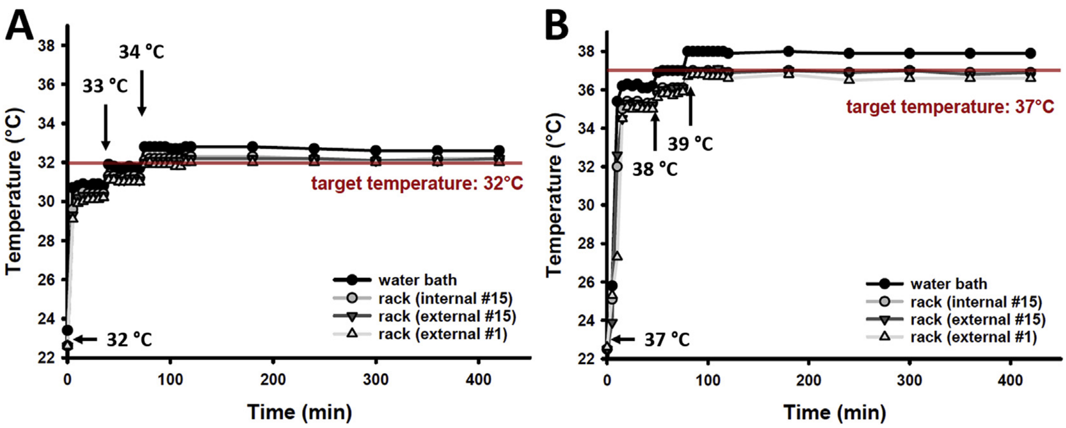

Fig. 2. Temperature distribution curves for set-points of 32 °C and 37 °C.A, the water bath was initially set to the desired target rack temperature of 32 °C. This resulted in an effective water bath temperature of 31 °C and a rack temperature of 30 °C. After 35 min, the water bath temperature was increased to 33 °C and finally (minute 70) to 34 °C, eventually achieving the target rack temperature of 32 °C. **B**, the same experiment was carried out for 37 °C. Target rack temperature was again achieved when water bath temperature was effectively at 38 °C (39 °C were set). The rate of heat loss, assuming an average water flow of 2 l/min calculates to 0.14 J/s.

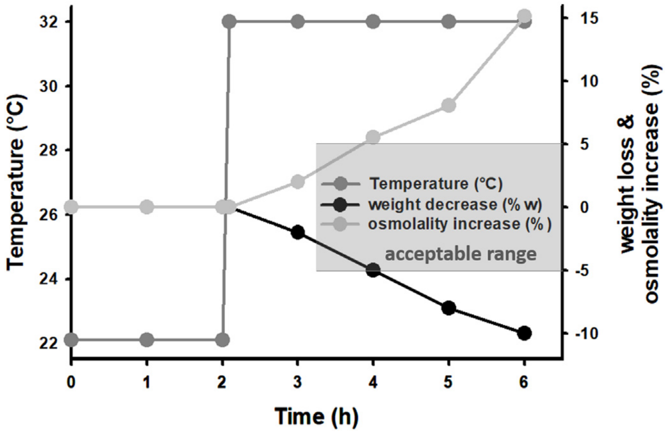

Fig. 3. Time course of solution evaporation and osmolality changes for RT and above.

While for 2 h at RT no changes in bath solution weight and osmolality were detectable, a subsequent increase to 32 °C revealed a weight loss of ~2.5 %w/h, progressing linearly with time. The resulting increase in relative osmolality due to loss of evaporating water from the wells was measured to be ~3.75%/h. A highlighted area marks the acceptable recording time span.

2.6. *Live analysis of MyoRobot 2.0 images compared to post-imaging analysis in image J*

In a final step to ultimately confirm the image analysis algorithm's capabilities, live images of EDL single fibers were taken to compare online analysis to post-processing in Image J. Fig. 6 shows four example fibers (identifier given in the top left corner) with their computed diameter and SL, determined via both techniques, *rising edge* and *FFT*, respectively. In white light images (*MyoRobot*), the sarcomere signal appears slightly out-of-focus and the fibers edges are blurry, which may be a reason for the *MyoRobot 2.0* algorithm to slightly overestimate fiber diameter here. Yet, since differences are mostly within the STDEV of the manual analysis, it can be concluded that discrepancies between both analysis methods are negligible, supporting the application of our edge and SL detection algorithm to live images and online analysis. The complete table (SI Table 2) comprised of 15 measured single fibers is found in the SI.

2.7. *Absolute fiber-to-sarcomere length relations confirm linear relationship, and single fiber RLT recordings starting from 2.6 μm SL confirm similar compliance and Young's modulus across fibers*

A typical mounting- and thus, absolute start resting-length L_0 in the previous *MyoRobot* system ranged between 1,800–2,100 μm. Therefore, we examined the sarcomere-to fiber-length relation in four different fibers that were either stretched or slackened after initial mounting and SL determination through the in-built optics. Fig. 7 clearly displays a linear relationship between SL and stretches or slackening in multiples of 50 μm absolute fiber length each, for all samples. Intriguingly, we could observe that the linear increase was similar across individual fibers, indicating that SL constantly increases (stretch) or decreases (slackening) at equal magnitude between 2.6 - 3.6 μm, regardless of initially mounted absolute fiber length.

This information was utilized to carry out resting-length-tension recordings (RLT) with SL adjusted to 2.6 ± 0.1 μm before each experiment. Using the *MyoRobot 2.0* optical system, we were able to derive the fiber diameter, allowing us to normalize forces to cross-sectional area, converting maximum passive restoration force (Fig. 8A) to maximum stress (Fig. 8B). While passive forces were measured to be 0.07 ± 0.01 mN, their specific force was in a range of 20 ± 5 kPa at average diameters of approx. 60 μm, resulting in ~3,000 μm^2 cross-sectional area (Fig. 8C). Fig. 8D displays passive axial compliance and Young's modulus. Both follow an expected inverse relationship with compliance showing a decreasing trend with strain while Young's modulus tends to increase.

3. Discussion

3.1. *Temperature-control of single fiber biomechatronics and reliable recording windows for ongoing experiments above 30 °C*

The improvement of the *MyoRobot* system for temperature-controlled recordings is a meaningful advancement. Temperature latency and heat loss due to imperfect hose isolation were compensated for. The resulting temperature was kept stable over hours and confirmed by multiple sensors to be homogeneously distributed throughout the rack via in-built turbulence chambers. An important assay was to assess evaporation under heated rack conditions. Here, a striking increase in osmolality of muscle fiber activating solutions was demonstrated already within 2 h when attempting to record at physiological temperatures (>30°C). On the short-term scale, it is recommended to either keep recording times above RT at a minimum (i.e. 2 hrs) or to perform series of different protocols sequentially. Yet, on the long-term scale, additional engineering solutions seem feasible. A possibility we currently envision is to engineer a vertical lid that either mechanically or electrically opens upon well exchange, allowing rack movement, and re-seals as soon as the pins emerge in active solution.

3.2. *Increased maximum force despite Ca^{2+} desensitization at higher temperatures*

In agreement with previous studies (Ranatunga and Wylie, 1983), recordings of temperature-dependent maximum force and caffeine-induced SR Ca^{2+} release force transients suggest at least two-fold increased force values for fibers recorded under physiological conditions (>30 °C, Fig. 4A). Here, absolute force measured 0.2 mN, which agrees with recordings done by Mendias et al. (2011) (Mendias et al., 2011). Caffeine-induced, Ca^{2+}-mediated force was observed to be approx. 2/3 of maximum active force for each respective temperature, which was expected at ~65% physiological endogenous SR filling (Lamb et al., 2001). Force transient amplitudes were more increased in proportion to maximum Ca^{2+} saturated force, arguing for a higher SR Ca^{2+} filling at elevated temperatures (at least referring to the Ca^{2+} releasable pool of total SR Ca^{2+}), similar to findings in isolated SR vesicles (Inesi et al., 1973). The increased maximum (Ca^{2+}-saturated) performance of fibers under warmed-up conditions likely appears to result from augmented cross-bridge cycling caused by higher actin-myosin binding turnover rates (de Tombe and Stienen, 2007; Wang and Kawai, 2001; Decostre et al., 2005). At high levels of activation (pCa = 4.92) and near physiological temperature, cross-bridge attachment and detachment rates are greatly enhanced (Zhao and Kawai, 1994) and both contribute to the overall tension development (de Tombe and Stienen, 2007). Further, temperature is assumed to boost the probability of state transitions during cross-bridge cycling, being a competent factor for isometric force generation (Decostre et al., 2005). This assumption could be verified by carrying out experiments on the speed of shortening, which is expected to result in faster performance at physiological conditions, as the ATPase activity of myosin determines the speed of muscle contraction (Bárány, 1967; Siemankowski et al., 1985). Further, for EDL maximum force generation, the Q10 temperature coefficient from 22 to 32 °C calculated to 2.46 aligns well with the reasonable physiological range for isometric contraction in fast-twitch muscle (Rall and Woledge, 1990). Experiments on rat EDL single fibers covering 25–35 °C yielded a Q10 of ~2.5 (Ranatunga, 1998), which agrees well with our results. Based on cross-bridge cycle modelling, the endothermic ATP hydrolysis was identified as contributor to the temperature-increased force generation, likely fuelling heat-absorbing force development (Offer and Ranatunga, 2015). These findings also point towards an increased

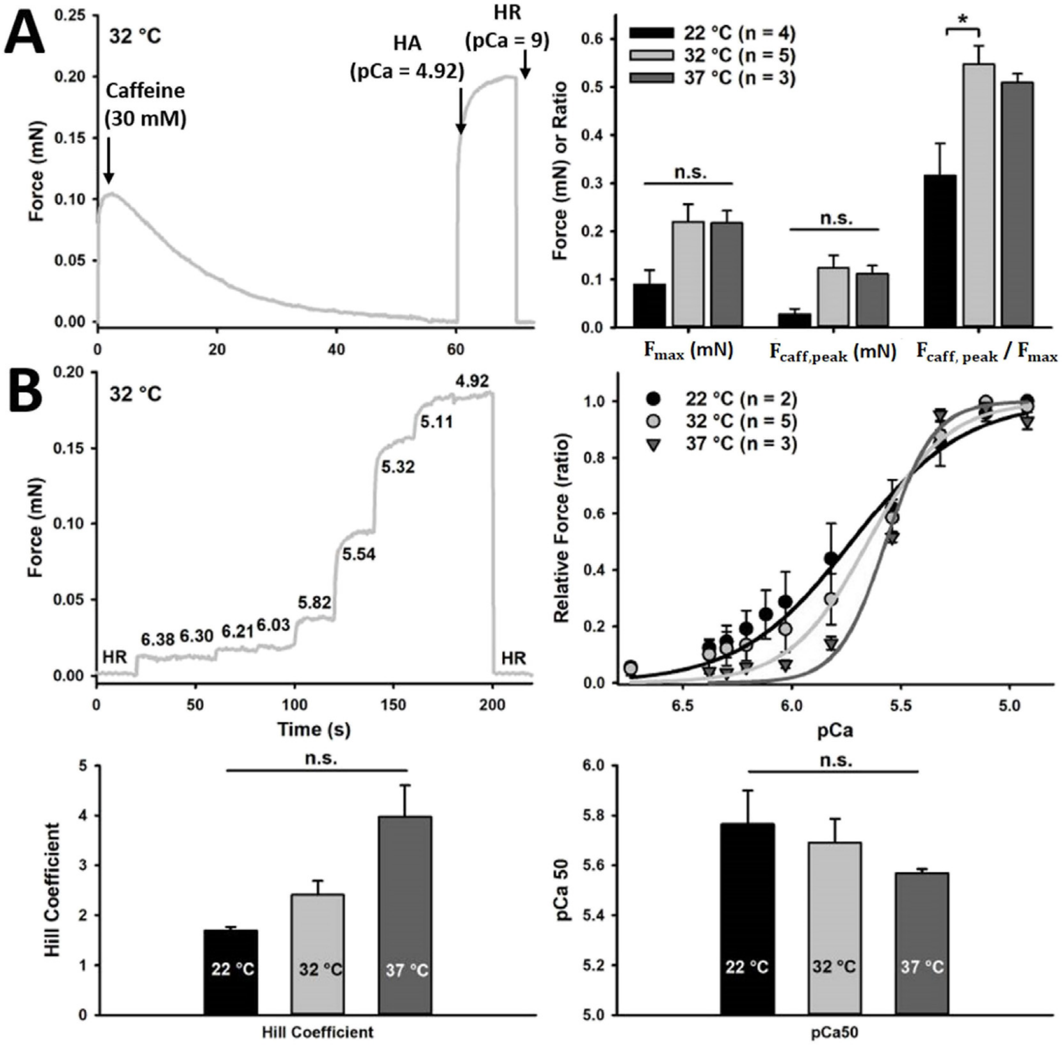

Fig. 4. Biomechanical performance of single muscle fibers at different physiological temperatures.A, example recording displaying a caffeine-induced force transient (F_{caff}) followed by maximum Ca^{2+} activation (F_{max}) of a single fiber at 32 °C. Analysis shows F_{max} to be approx. two-fold increased for recordings above RT, while the peak of F_{caff} ($F_{caff,peak}$) is even more increased. This trend explains the resulting higher ratio of both values for temperatures above RT, in which warmed up fibers once again outperform their RT counterparts. **B**, displays a representative recording of a pCa-force curve at 32 °C, flanked by force relaxation to ~0 mN in HR solution. Decreasing pCa steps are marked in the plot. The group analysis for all temperatures is shown on the right, including group fits obtained by averaging all fit values of single recordings. While curve steepness (Hill-coefficient) constantly increases with temperature, the fits reveal a right-shift towards smaller pCa_{50} values. Both, average Hill-coefficient and pCa_{50} value, are presented in the bar charts below. *: $p<0.05$; n.s.: not significant.

SERCA1 Ca^{2+} pump activity at higher temperatures. Indeed, in chemically stimulated human *vastus lateralis* and *rectus abdominis* fibers, SR Ca^{2+} ATP hydrolysis is reported to reveal a Q10 of 2.6 from 12 to 30 °C, which is proposed to be less augmented than the Q10 value of isometric peak force amplitudes (Stienen et al., 1996).

Evaluation of pCa-force curves displays a two-fold increased Hill coefficient for fibers recorded at 37 °C in comparison to RT, indicating a narrowed dynamic range at 37 °C. This suggests a higher stoichiometric number of Ca^{2+} ions binding to troponin-C per force unit increase. However, literature implies that Ca^{2+} sensitivity and Hill coefficient may not directly correlate with the number of Ca^{2+} ions binding to regulatory proteins (Brenner, 1988; Landesberg and Sideman, 1994). The basis of this assumption originates from two parameters, f and g, that were first introduced by Huxley and Simmons (1971). (Huxley and Simmons, 1971) as rate constants to describe two distinct cross-bridge turnover states. Here, f refers to a transition from a non-force to a force generating state while g reflects the opposite transition (ADP release and ATP binding). Those were utilized in Brenner (1988) (Brenner, 1988) to describe cross-bridge turnover kinetics. By combining Ca^{2+} sensitivity protocols with ATPase related NADH absorption spectroscopy, they concluded that a large Hill coefficient does not necessarily point towards long-range cooperativity of Ca^{2+} binding sites at troponin-C, but may arise due to an increased f/g ratio (Brenner, 1988). Therefore, the steeper pCa-force curves recorded above RT likely are a consequence of increased actomyosin ATPase turnover rates due to an enhanced transition from a non-force to a force generating state, rather than augmented Ca^{2+} binding sites.

In contrast to curve steepness, the pCa_{50} value decreased with temperature, implying a desensitization of the contractile apparatus. Quantifying the decrease of pCa_{50} per 1 °C results in $\Delta pCa = 0.012 \frac{pCa}{1^{o}C}$ and agrees with the decrease found in skinned EDL single fibers of rats (Stephenson and Williams, 1985). With increasing temperature, the Ca^{2+} affinity of troponin-C is reduced due to negative binding enthalpy and thus, likely responsible for the observed Ca^{2+} desensitization. Further studies on frog muscle fibers report a similar temperature-dependent decrease in pCa_{50} and moreover, emphasise a parallel increase in maximum force (Godt, 1982), which supports our observations. A more detailed analysis yields that at high Ca^{2+} concentration ($pCa = 5.0$), an increase in temperature caused greater maximum force generation, while at lower Ca^{2+} containing solutions ($pCa = 5.8$), force

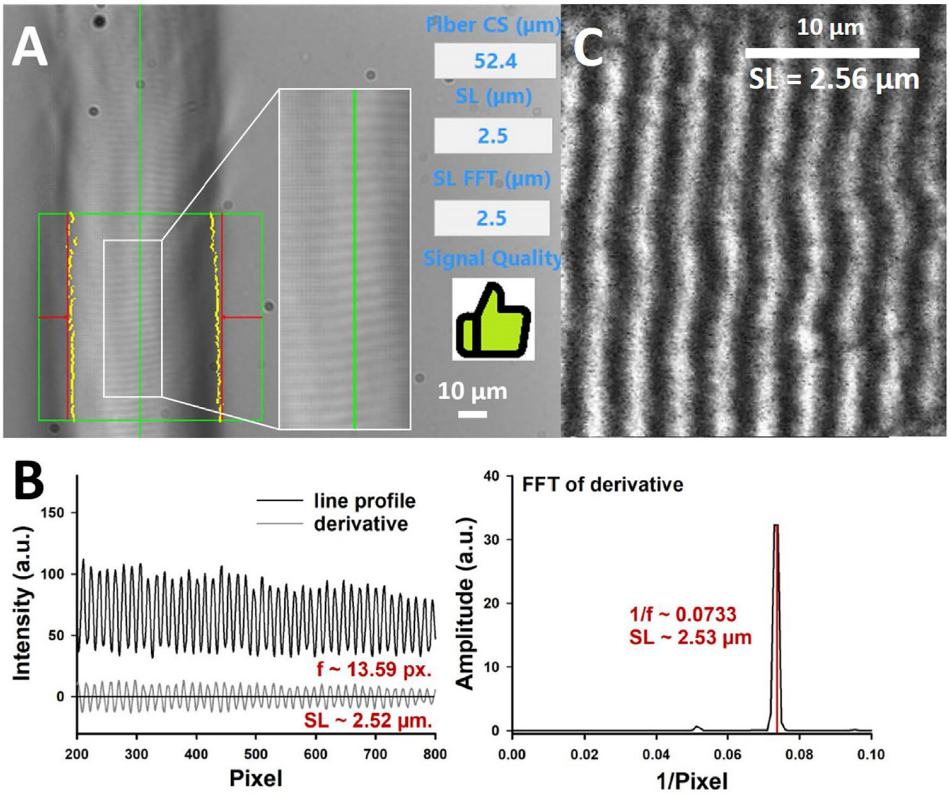

Fig. 5. Validation of the accuracy of the *MyoRobot 2.0*-implemented optics and *MyoWizard* SL detection algorithm based on SHG images of the exact same EDL single fiber.A, shows an EDL single fiber visualized with the *MyoRobot 2.0* optics. The image area framed by the green box was used for edge detection (results indicated by red lines; edges meeting the criteria are marked with yellow dots) and the line profile for SL calculation was obtained along the green line. The sarcomere pattern is magnified in the white box. Our *MyoWizard* measured a fiber diameter of 52.4 μm and a SL of 2.5 μm for both computation methods detailed in **B**. The *rising edge* technique utilized the derivative of the line profile to search for rising edges whose distances were converted to a physical average for sarcomere spacing (red numbers in plot). In parallel, a FFT of the repetitive pattern of the derivative resulted in a single peak in the 1/px. domain. Maximum detection then allowed a conversion to the μm scale. **C**, high resolution SHG image of the same EDL fiber as in (**A**) after *MyoRobot 2.0* evaluation. Analysis of the 3D SHG image stack yields an average SL of 2.56 μm, matching well with the results obtained with our *MyoRobot 2.0* algorithm. (For interpretation of the references to colour in this figure legend, the reader is referred to the Web version of this article.)

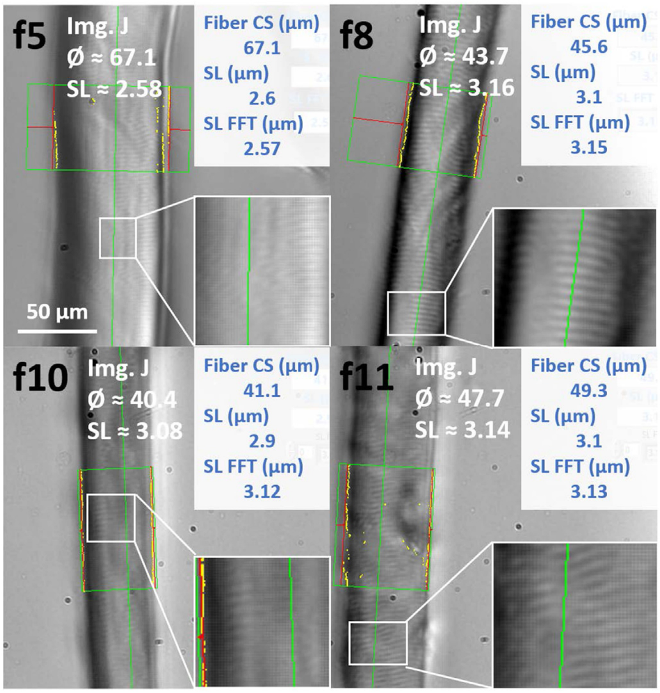

Fig. 6. Images of wt EDL single fibers taken and analyzed with the *MyoRobot 2.0* optical system *on-the-fly* (blue), including comparative values obtained in Image J (white).

Four different single fibers are displayed (f5, f8, f10 and f11, see Table 2 (SI) for further details) along with the results obtained from the *MyoRobot 2.0* algorithm in grey boxes. Comparative values by manual analysis in Image J given in white. Scale bar applicable to all images. (For interpretation of the references to colour in this figure legend, the reader is referred to the Web version of this article.)

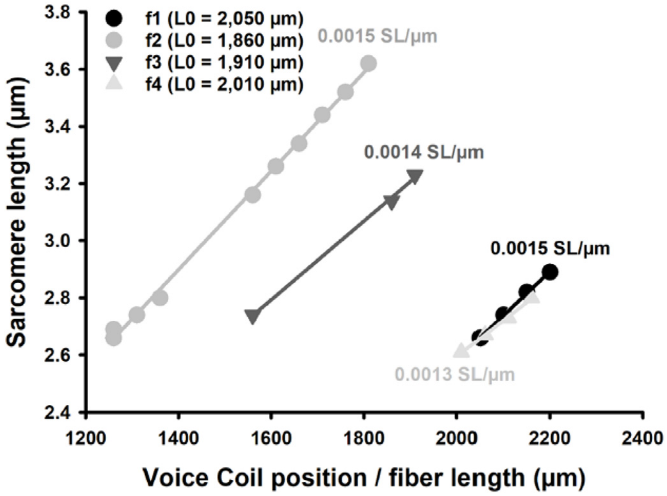

Fig. 7. Sarcomere length-to-absolute fiber length relation reveals proportionality.

Four single muscle fibers were mounted at the given resting length L_0 to impose changes in absolute fiber length via VC actuation in steps of 50 μm. SL was analyzed using the *MyoRobot 2.0* optical system and detection algorithm, revealing a linear relationship between SL and VC position change.

declined (Godt, 1982) at higher temperature. Thus, this enhanced difference between increased force values at pCa <5.0 and reduced forces at pCa >5.8 provide an explanation for the enhanced force-pCa curve steepness.

3.3. Accurate resolution and SL detection with the MyoRobot 2.0 in-built optical system

Utilizing the USAF (1951) target, resolution was verified to resolve structures of at least ~2.193 μm, corresponding to the smallest element

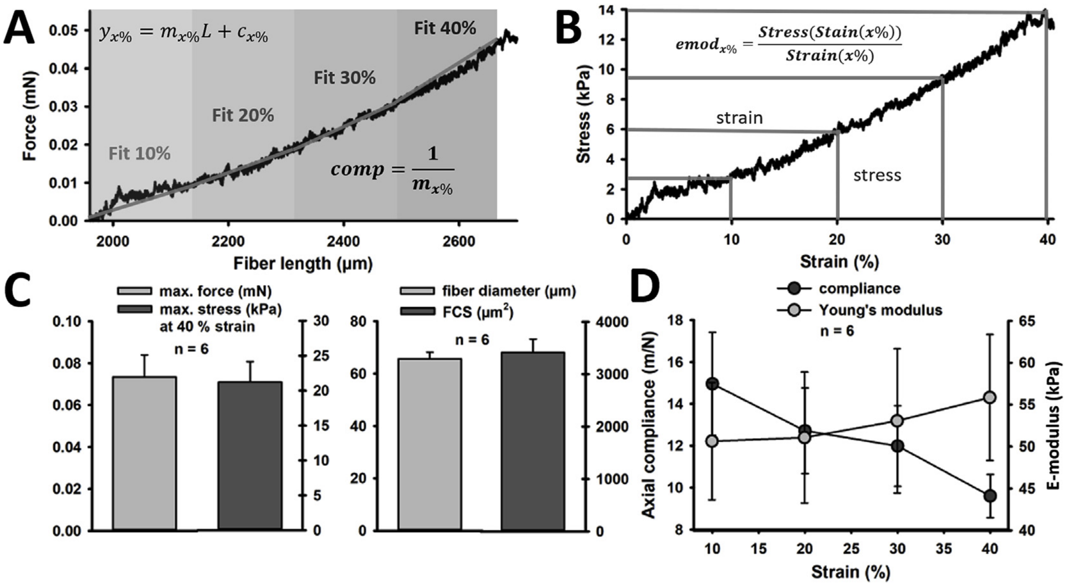

Fig. 8. RLT curves from single muscle fibers starting at 2.6 μm SL reveal decreasing compliance and increasing Young's modulus with strain. Representative plots of an RLT-curve displayed as force-fiber-length (**A**) and stress-strain relation (**B**). Axial compliance was derived from the force-length relation by applying linear fits to each section of 10% length change and calculating the inverse increase. The Young modulus was computed from the stress-strain relation by dividing the stress at a given strain by the respective strain. **C**, maximum force of single fibers and calculated maximum passive stress. To the right, average fiber diameter and resulting FCS (assuming circular cross section) are presented. **D**, axial compliance and Young's modulus tend to decrease and to increase, respectively, with strain.

on the target which was still easily resolved. Since line pairs were still distinguishable, the assumption of resolving sarcomeres in the range of 1.6–3.6 μm was confirmed with live images. Comparing SHG processed image stacks to single white light image analysis performed on the same single fiber with the *MyoRobot 2.0* optics and software suggests a good match between results for fiber diameter and SL (Table 1). The expanded live analysis of single fibers validates the correct detection of both values online, but suggests that the *FFT* detection method is better suited for images with low contrast or compromised signal quality.

3.4. Linear absolute fiber-to-sarcomere length relation across various mounting distances

As expected, linear changes to absolute fiber length L_0 implied linear changes in SL over a long range ($\Delta L \sim 600\,\mu m$); yet, intriguingly different mounting distances did not affect the proportionality factor, being at $\sim 0.0014\,\mu m SL/\mu m L_0$ across preparations. Although at shorter mounting distance, a stretch of 50 μm should represent a greater relative elongation than at longer mounting distances, our results suggest that between an initial pin distance of 1,800–2,100 μm, SL follows absolute fiber length in a robust, linear fashion.

3.5. Automated assessment of steady-state axial compliance and elasticity modulus in single fibers

Active length-tension relationships display a plateau for maximum force generation between 2.0 - 2.4 μm (Gordon et al., 1966a, 1966b; Edman, 2005) before force declines. This is due to the passive elements stiffening for SL ≥2.6 μm (ter Keurs et al., 1978), reflecting the descending limb of the active length-tension relationship. Since this dependence varies from species to species (Rassier et al., 1999), SL must be precisely controlled to map the descending limb in murine muscle (2.6 μm (Edman, 2005)) prior to recording passive restoration force, axial compliance and Young's modulus.

Due to the technical complexity of investigations regarding the passive elements, i.e. limited availability of commercial biomechatronics systems allowing high precision automated quasi-static pull, only few data are available on passive restoration forces, in particular for single fibers. Experiments on whole muscles suggest specific passive force values between 200 and 400 kPa (Smith and Barton, 2014); nevertheless, direct comparability of absolute values to other organ scales is compromised due to the strong dependence on preparation geometry and either presence or absence of extracellular matrix (ECM). The scarce data available on single fibers yields values of 40–60 kPa (Anderson et al., 2001, 2002) in murine *soleus* muscle (a typical slow-twitch muscle). Assuming a two-fold increased passive restoration force in *soleus* over EDL fibers, as reported for rat in Mutungi and Ranatunga (1996) and similarly in mouse muscle (Haug et al., 2018), our observed EDL single fiber specific passive force (elastic stiffness) of 20 ± 5 kPa clearly is in a reasonable range. Further support is provided by investigations in murine wt *soleus* fiber bundles, revealing a specific restoration force of approx. 60 kPa after a stretch to 3.5 μm SL (Diermeier et al., 2017b), proposing the EDL to display about 30 kPa, which was confirmed in our recordings.

Recent studies on *soleus* suggested single fiber diameters to be 30–40 μm (Diermeier et al., 2017a), while EDL fibers reveal a larger diameter of 38–75 μm which is however, strongly dependent on fiber type (Alnaqeeb and Goldspink, 1987). Assuming circular cross section, our values for cross-sectional area (~3,000 μm^2) scale well with an average fiber diameter of 60 μm.

The Young modulus revealed an increasing trend from 45 to 55 kPa with strain. This range is also reflected in developing C2C12 myoblasts (Collinsworth et al., 2002) and is further comparable to other muscle types (Mathur et al., 2001) investigated with atomic force microscopy (AFM). The apparent Young modulus of myotube membrane was found to be ~45 kPa (Collinsworth et al., 2002), which was confirmed by AFM in fully developed muscle cells (40–60 kPa at 60–80 nm indentation) and agrees with our results regarding isolated single muscle fibers. However, it must be kept in mind that indentation and axial strain reflect two different biomechanical stressors yielding lateral and axial elasticity modules, respectively. The former includes more the lateral traction forces including the ECM (if present), membrane and dystroglycan complex as well as its connection to cytoskeletal components (Collinsworth et al., 2002), while the latter reflects the sarcomeric and extra-sarcomeric longitudinal cytoskeletal components, i.e. titin (Granzier and Irving, 1995). Nevertheless, we conclude that adjusting SL to 2.6 μm (decreasing limb of the length-tension relation) is beneficial to obtain comparable and physiologically relevant results, and to produce a more reproducible and coherently defined state of the muscle fiber preparation to relate the biomechanical results to.

In contrast to the Young's modulus, axial compliance minimally decreases in gradually elongated EDL single fibers. The axial compliance range of 10–16 m/N is smaller than values found in fiber bundles (Haug et al., 2018). The more compliant behaviour of single fibers is likely due to the lack of ECM and a therefore, reduced tensile contribution to passive resistance. The ECM of muscle fibers represents a functional extension of the tendon (Wood et al., 2014) and bears the majority of passive load (Gillies and Lieber, 2011). Therefore, it is not surprising that elastic stiffness of fiber bundles is more than two-fold augmented compared to single fibers (Gillies and Lieber, 2011; Meyer and Lieber, 2011). Comparing our single fiber results with a previous assessment of passive force in bundles (Haug et al., 2018) revealed similar results. Considering that ECM only takes up ~18% fraction of cross-sectional area (Wood et al., 2014), it can be assumed to be an extremely stiff scaffold surrounding rather compliant fibers. Consequently, in stress-strain relations, single muscle fibers void of their ECM display a linear relation, such as observed here, while fiber bundles present non-linear behaviour due to ECM presence (Gillies and Lieber, 2011).

3.6. Summary and outlook

Above all, improvements enabling temperature and SL adjustment were verified to work accurately and to markedly increase the versatility of applications of our improved *MyoRobot 2.0* system for advanced biomechanics investigations. Compensating temperature latency and loss was accounted for to stably maintain the desired temperature at the preparation. Results regarding temperature-dependent Ca^{2+} sensitivity revealed a desensitization at physiological temperatures. Future biological applications involving more specific animal models will help to establish a larger database to approximate systematic fluctuations in data distributions.

The most meaningful advancement of our *MyoRobot 2.0* system was the inclusion of an infinity optics for *on-the-fly* optical assessment of fiber geometries (diameter, SL). This approach rendered our biomechatronics solution independent of external research microscopes, unlike other commercial systems, and combines opto-mechatronics communication in one system. In-built SL adjustment will make a great contribution to standardization in single fiber biomechanics. The passive properties of EDL single muscle fibers at their descending limb from 2.6 μm match well with published results, highlighting the necessity of SL adjustment prior to any assessment of passive elasticity/compliance. Thus, the enhanced *MyoRobot 2.0* system has proven to be a valuable platform for carrying out advanced biomechanical experiments. The now implemented control over temperature and SL, while providing force normalization to fiber cross section *on-the-fly* makes it superior to other systems on the market and makes it an attractive system for upcoming commercialization.

4. Materials and methods

4.1. MyoRobot 2.0 hardware components

Since the introduction of the system in Haug et al. (2018) (Haug et al., 2018), it was expanded by multiple features (Fig. 1), increasing its automation range and versatility to include modular protocol packages for state-of-the-art biomechanics research and biopolymer testing. Amongst these, temperature controlled recordings were enabled by constructing a heated multi-well rack made of stainless steel. Liquid heating allowed the use of space saving fluid connectors and hoses to easily link the rack to any typical water bath for reliable temperature control. For each new bath reservoir and hose-connector combination, an initial calibration would be required to relate set water bath temperature to measured rack heat. Homogeneous temperature distribution was realized by in-built turbulence chambers (Fig. 1B) while an integrated platinum resistance heat thermistor (HEL-700, Honeywell) at well #15 monitored internal rack temperature, which was digitized using the Pt1000 transmitter (B + B SENSORS). For temperature calibration, two additional external multimeter sensors were applied at position #15 and #1 of the temperature-controlled rack.

Due to the steel rack possessing a tare weight of 534 g, the previous stepper motors had to be replaced by a more powerful alternative, namely ballscrew linear actuators. Those still work at 400 mm/s if the payload is below 1 kg. Therefore, the vertical axis was replaced with the RCP3-SA4R and the horizontal axis by the RCP4-SA3C, manufactured by IAI America, Inc. and featuring customizable velocity control, position referencing at a resolution of ±0.02 mm while appraised long life expectancy and low power consumption. The motors were linked to PCON-CA controllers (IAI America, Inc.), providing software communication based on a LabVIEW controlled interface and allowing position feedback and a fully re-writable position parameter storage.

Further, optical access to the sample was granted by sealing the rack with a glass bottom and implementing a custom-built microscope optics, tailored for the narrow space and application within the *MyoRobot 2.0* system (Fig. 1C). The system is basically composed of a 20 mm focus lens, a 500 mm tube lens and two tilting mirrors (LA1859-A and LA1908-A, BB1-E02 and DMLP605, THORLABS) providing a magnification of ~24 x. The focus lens and the first tilting mirror were placed below the sample, mounted on a custom-built vertical holder, including a micrometer screw for manual focus adjustment. Driving the lens in a way that its back focal length aligned with the sample resulted in parallel rays exiting the focus lens before deflecting them by 90^o via the first mirror. Consequently, they passed the tube lens and hit the second mirror being placed in a THORLABS kinematic mount, for easy field-of-view fine adjustment, followed by the CCD camera (DFK 61BUC02, The Imaging Source). All optical parts were fixed on alignment post holders mounted on a rail system fabricated in our institute workshop. The transmission light source being adjustable in position, was composed of a flash light (P4, LED Lenser).

4.2. Software and edge/SL detection implementation

Actuation control of linear motors and VC actuator was realized in a customizable tabulator control panel including save and load functionality within the *MyoRobot 2.0* GUI, we name *MyoWizard*. Predefined recording protocols to execute routines such as pCa-force or RLT curves could be loaded, modified and saved in a table containing well number # and dwell time t#, while more advanced options for VC actuation were customizable in a separate window, allowing to set a delay time prior to changes of absolute mounted fiber length L_0, the actual change in L_0 or the time to reside in this new position. FT data were continuously monitored on a signal diagram. Buttons enabled skipping or pausing the current execution sequence or terminating the protocol prematurely. To facilitate fiber mounting, a manual mode was accessed to operate the vertical motor to elevate or lower the FT and VC pin, as well as changing pin distance using the arrow keys on the control keyboard.

The *MyoRobot 2.0* camera control software (*MyoWizard*) features buttons to adjust camera properties, such as BCG values, exposure and gain to acquire a contrast-rich image. Fiber edge detection was implemented using the standard LabVIEW function that projected a green search rectangle onto the image, whose edges and rotation were adjusted via slider controls. The function scanned for contrast differences of defined magnitude within the rectangle. Edge distances are derived in pixel values and converted to physical μm by multiplication with the camera voxel size. Determining SL was done by obtaining the intensity profile along a line, whose position and orientation were derived from the rectangles coordinates. By calculating the discrete derivative, sharp contrast changes were transformed into amplitudes and sarcomere distance (maximum intensities) were reflected as rising edges passing the horizontal zero line. Based on optimization steps, a filtering function excluded sections of $amp. < 1\ int/px.$ and distances not matching a physiological SL range of $1.5 - 5\,\mu$m. Consequent averaging and obtaining the median of all distances allowed to derive a reliable value for online SL determination. For further back up, the derivative was transformed into the Fourier domain via FFT, in which repetitive patterns at certain frequency become visible as distinguished peaks along the power spectrum. Applying similar filter functions and implementing three thresholding techniques (*half max.*, *95% quantile* or *manual*) allowed for automated peak detection, whose location was re-transformed, displayed to the user and ultimately compared with the rising-edge method.

4.3. Camera calibration, resolution and algorithm validation experiments

Camera calibration was done using elements on a USAF (1951) target of different line width (15.61 and 6.96 μm for G5E1 and G6E2, respectively). An image of each element was saved to disk using the *MyoRobot 2.0* software and analyzed in Image J by five-times measuring each line of the element (SI Fig. 9A). Knowing the distance in pixel and physical line width, the ratio reflected the camera CF and was determined to be 0.14 μm/px.

Obtaining the resolution power required to image the smallest element of the UASF (1951) target, which was G7E6 featuring 228 line pairs per 1 mm. Using the *MyoRobot 2.0* optics, the element was easily resolved, suggesting a resolution of at least $< \frac{1000\mu m}{228lp * 2} < 2.193\mu m$ (SI Fig. 9B).

To validate the optical SL determination, single muscle fibers were fixed in a well containing 4% PFA at a given SL and then imaged using the *MyoRobot 2.0* optics. The preserved fibers where then transferred to a Vaseline bedded coverslip for SHG microscopy while their SL remained fixed to the value measured in the *MyoRobot 2.0*. A mode-locked 800 nm ps-pulsed Ti:Sa laser (Chameleon Vision II, Coherent, Santa Clara, CA, USA) was used for SHG microscopy (TriMScope II, LaVision BioTec, Bielefeld, Germany) to excite the second harmonic generation (SHG) signal of myosin. The fluorescence signal at 405 nm was detected as forward scattered signal to create a 3D volume with single slices being 0.5 μm apart (step-size). For further details refer to (Diermeier et al., 2017b). Image stacks of the exact same fibers were analyzed with an Image J plugin (Fiji) providing a measure for average SL based on FFT. Ultimately, SHG derived values were compared to *MyoWizard* results. Then, the algorithm was tested during live *MyoRobot 2.0* recordings and automated *MyoWizard* analysis against manual measurements in Image J. For this, fifteen fibers were analyzed to determine SL and fiber diameter, while .tif images were stored to disk for comparative post-imaging analysis with Image J (no plugin). Five-times repeated line measurements were carried out. The results are correlated to the *MyoWizard* obtained values in Fig. 7 and confirm the algorithm to be applicable for *on-the-fly* use.

4.4. Single muscle fiber preparation

To validate the newly developed features of the *MyoRobot 2.0*, murine EDL single fibers were used. Further details regarding the preparation and use of chemical solutions are given in the SI Methods.

4.5. Chemically and mechanically driven recording protocols

Prior to any recording, single muscle fibers were immersed for 20 s in chemical skinning solution (saponin 0.01% w/v), emptied of internal releasable sarcoplasmic Ca^{2+} by exposure to RS (containing 30 mM caffeine) for 60 s followed by another 60 s in HR to remove any excess Ca^{2+} before returning to the idle (LR) well. Solutions used for preparation or muscle activation/relaxation were composed as in Haug et al. (2018) (Haug et al., 2018). The following recording procedures were implemented:

(1) *Maximum force and caffeine-induced force transients:* emptied of endogenous Ca^{2+}, the SR of single fibers was reloaded under defined conditions and followed by caffeine-induced SR Ca^{2+}-release. Maximum Ca^{2+} saturated force generation terminated the protocol: 90 s LS - 1 s HR - 60 s LR - 90 s RS - 10 s HA - 60 s HR. The chosen sequence was optimized in loading time to achieve a caffeine-induced force amplitude of ~2/3 maximum force. Results are presented in Fig. 4A.

(2) *Ca^{2+} sensitivity of the myofibrillar contractile apparatus:* the permeabilized sample was directly exposed to wells with sequentially decreasing pCa value, composed of highly-EGTA buffered relaxing and Ca^{2+} rich activating solution. Each immersion lasted for 20 s before proceeding to the next well (Fig. 4B).

(3) *Absolute fiber-to-sarcomere-length relation:* fibers were mounted between 1,800–2,100 μm L_0 and resting SL determined via the *MyoRobot 2.0* software. Subsequently, the VC was driven in steps of multiples of 50 μm to stretch or relax the fiber and obtain its SL in dependence of its new absolute length to which linear slopes were fitted (see (Haug et al., 2018)).

(4) *Passive axial compliance in resting-length-tension curves starting from 2.6 μm SL:* addressing the fibers passive axial compliance under relaxing LR conditions required constant and slow stretching at velocities ensuring a steady-state between instantaneous elastic restoration force and viscous relaxation. This was implemented by driving the VC at ~0.42 μm/s to stretch the fiber to 140% L_0, after initially calibrating its SL to 2.6 ± 0.1 μm. An example of an RLT experiment is depicted in Fig. 8A.

A detailed description to data analysis regarding calcium sensitivity and RLT recordings is given in the SI Methods.

Author contributions statement

M.H., C.M., and B.R. conducted the experiments. M.H. and C.M. analyzed the results. M.H., C.M., G.P. S.R. and M. Heckel engineered the *MyoRobot 2.0* biomechatronics system. S.N., D.S. and S.S. provided analysis tools and results interpretation. O.F. conceived the project and supervised the whole research. M.H., C.M., T.P. and O.F. wrote the manuscript. All authors approved the manuscript.

Competing interests

The authors disclose project partnership with the SME conmoto GbR through the aforementioned R&D grant.

Conflict of interest

The authors declare that there is no conflict of interest.

Acknowledgements

This work was supported by a grant from the Central Innovation Program SME of the German Ministry of Economy & Technology (ZIM-Kooperationsprojekt KF2347924AK4) to O.F.

Appendix A. Supplementary data

Supplementary data to this article can be found online at https://doi.org/10.1016/j.bios.2019.04.052.

References

Alnaqeeb, M.A., Goldspink, G., 1987. Changes in fibre type, number and diameter in developing and ageing skeletal muscle. J. Anat. 153, 31–45.

Anderson, J., Li, Z., Goubel, F., 2002. Models of skeletal muscle to explain the increase in passive stiffness in desmin knockout muscle. J. Biomech. 35 (10), 1315–1324.

Anderson, J., Li, Z., Gouble, F., 2001. Passive stiffness is increased in soleus muscle of desmin knockout mouse. Muscle Nerve 24 (42), 1090–1092.

Bárány, M., 1967. ATPase activity of myosin correlated with speed of muscle shortening. J. Gen. Physiol. 50 (6), 197–218.

Berchtold, M.W., Brinkmeier, H., Müntener, M., 2000. Calcium ion in skeletal muscle: its crucial role for muscle function, plasticity, and disease. Physiol. Rev. 80 (3), 1215–1265.

Bigland, B., Zaimis, E., 1958. Factors influencing limb temperature during experiments on skeletal muscle. J. Physiol. 141 (3), 420–424.

Brenner, B., 1988. Effect of Ca2+ on cross-bridge turnover kinetics in skinned single rabbit psoas fibers: implications for regulation of muscle contraction. Proc. Natl. Acad. Sci. U. S. A 85 (9), 3265–3269.

Collinsworth, A.M., Zhang, S., Kraus, W.E., Truskey, G.A., 2002. Apparent elastic modulus and hysteresis of skeletal muscle cells throughout differentiation. Am. J. Physiol. Cell Physiol. 283 (4), C1219–C1227.

de Tombe, P.P., Stienen, G.J.M., 2007. Impact of temperature on cross-bridge cycling kinetics in rat myocardium. J. Physiol. 584 (Pt 2), 591–600.

Decostre, V., Bianco, P., Lombardi, V., Piazzesi, G., 2005. Effect of temperature on the working stroke of muscle myosin. Proc. Natl. Acad. Sci. U. S. A 102 (39), 13927–13932.

Diermeier, S., Buttgereit, A., Schürmann, S., Winter, L., Xu, H., Murphy, R.M., Clemen, C.S., Schröder, R., Friedrich, O., 2017a. Preaged remodeling of myofibrillar cytoarchitecture in skeletal muscle expressing R349P mutant desmin. Neurobiol. Aging 58, 77–87.

Diermeier, S., Iberl, J., Vetter, K., Haug, M., Pollmann, C., Reischl, B., Buttgereit, A., Schürmann, S., Spörrer, M., Goldmann, W.H., Fabry, B., Elhamine, F., Stehle, R., Pfitzer, G., Winter, L., Clemen, C.S., Herrmann, H., Schröder, R., Friedrich, O., 2017b. Early signs of architectural and biomechanical failure in isolated myofibers and immortalized myoblasts from desmin-mutant knock-in mice. Sci. Rep. 7 (1), 1391.

Ebashi, S., 1976. Excitation-contraction coupling. Annu. Rev. Physiol. 38, 293–313.

Edman, K.A.P., 2005. Contractile properties of mouse single muscle fibers, a comparison with amphibian muscle fibers. J. Exp. Biol. 208 (Pt 10), 1905–1913.

Friedrich, O., Yi, B., Edwards, J.N., Reischl, B., Wirth-Huecking, A., Buttgereit, A., Lang, R., Polyak, F., Liu, I., Wegner, F. v., Cully, T.R., Lee, A., Most, P., Voelkers, M., 2014. IL-1alpha reversibly inhibits skeletal muscle ryanodine receptor. a novel mechanism for critical illness myopathy? Am. J. Respir. Cell Mol. Biol. 50 (6), 1096–1106.

Gillies, Allison R., Lieber, Richard L., 2011. Structure and function of the skeletal muscle extracellular matrix. Muscle Nerve 44 (3), 318–331.

Godt, R.E., 1982. Influence of temperature upon contractile activation and isometric force production in mechanically skinned muscle fibers of the frog. J. Gen. Physiol. 80 (2), 279–297.

Gordon, A.M., Huxley, A.F., Julian, F.J., 1966a. Tension development in highly stretched vertebrate muscle fibres. J. Physiol. 184 (1), 143–169.

Gordon, A.M., Huxley, A.F., Julian, F.J., 1966b. The variation in isometric tension with sarcomere length in vertebrate muscle fibers. J. Physiol. 184, 170–192.

Granzier, H.L., Irving, T.C., 1995. Passive tension in cardiac muscle: contribution of collagen, titin, microtubules, and intermediate filaments. Biophys. J. 68 (3), 1027–1044.

Haug, M., Reischl, B., Prölß, G., Pollmann, C., Buckert, T., Keidel, C., Schürmann, S., Hock, M., Rupitsch, S., Heckel, M., Pöschel, T., Scheibel, T., Haynl, C., Kiriaev, L., Head, S.I., Friedrich, O., 2018. The MyoRobot: a novel automated biomechatronics system to assess voltage/Ca2+ biosensors and active/passive biomechanics in muscle and biomaterials. Biosens. Bioelectron. 102, 589–599.

Head, S.I., 2010. Branched fibres in old dystrophic mdx muscle are associated with mechanical weakening of the sarcolemma, abnormal Ca2+ transients and a breakdown of Ca2+ homeostasis during fatigue. Exp. Physiol. 95 (5), 641–656.

Huxley, A.F., Simmons, R.M., 1971. Proposed mechanism of force generation in striated muscle. Nature 233 (5321), 533–538.

Inesi, G., Millman, M., Eletr, S., 1973. Temperature-induced transitions of function and structure in sarcoplasmic reticulum membranes. J. Mol. Biol. 81 (4), 483–504.

Lamb, G.D., Cellini, M.A., Stephenson, D.G., 2001. Different Ca2+ releasing action of caffeine and depolarisation in skeletal muscle fibres of the rat. J. Physiol. 81 (531), 715–728.

Lamb, G.D., Stephenson, D.G., 2018. Measurement of force and calcium release using mechanically skinned fibers from mammalian skeletal muscle. J. Appl. Physiol. 125 (4), 1105–1127.

Landesberg, A., Sideman, S., 1994. Coupling calcium binding to troponin C and cross-bridge cycling in skinned cardiac cells. Am. J. Physiol. 266 (3 Pt 2), H1260–H1271.

Lännergren, J., Westerblad, H., 1987. The temperature dependence of isometric contractions of single, intact fibres dissected from a mouse foot muscle. J. Physiol. 390, 285–293.

Mathur, A.B., Collinsworth, A.M., Reichert, W.M., Kraus, W.E., Truskey, G.A., 2001. Endothelial, cardiac muscle and skeletal muscle exhibit different viscous and elastic properties as determined by atomic force microscopy. J. Biomech. 34 (12), 1545–1553.

Mendias, C.L., Kayupov, E., Bradley, J.R., Brooks, S.V., Claflin, D.R., 2011. Decreased specific force and power production of muscle fibers from myostatin-deficient mice are associated with a suppression of protein degradation. J. Appl. Physiol. 111 (1), 185–191.

Meyer, G.A., Lieber, R.L., 2011. Elucidation of extracellular matrix mechanics from muscle fibers and fiber bundles. J. Biomech. 44 (4), 771–773.

Mutungi, G., Ranatunga, K.W., 1996. The viscous, viscoelastic and elastic characteristics of resting fast and slow mammalian (rat) muscle fibres. J. Physiol. 496 (3), 827–836.

Offer, G., Ranatunga, K.W., 2015. The endothermic ATP hydrolysis and crossbridge attachment steps drive the increase of force with temperature in isometric and shortening muscle. J. Physiol. 593 (8), 1997–2016.

Rall, J.A., Woledge, R.C., 1990. Influence of temperature on mechanics and energetics of muscle contraction. Am. J. Physiol. 259 (2 Pt 2) R197–203.

Ranatunga, K.W., 1998. Temperature dependence of mechanical power output in mammalian (rat) skeletal muscle. Exp. Physiol. 83 (3), 371–376.

Ranatunga, K.W., Wylie, S.R., 1983. Temperature-dependent transitions in isometric contractions of rat muscle. J. Physiol. 339, 87–95.

Rassier, D.E., MacIntosh, B.R., Herzog, W., 1999. Length dependence of active force production in skeletal muscle. J. Appl. Physiol. 86 (5), 1445–1457.

Sam, M., Shah, S., Fridén, J., Milner, D.J., Capetanaki, Y., Lieber, R.L., 2000. Desmin knockout muscles generate lower stress and are less vulnerable to injury compared with wild-type muscles. Am. J. Physiol. Cell Physiol. 279 (4), C1116–C1122.

Siemankowski, R.F., Wiseman, M.O., White, H.D., 1985. ADP dissociation from actomyosin subfragment 1 is sufficiently slow to limit the unloaded shortening velocity in vertebrate muscle. Proc. Natl. Acad. Sci. U. S. A 82 (3), 658–662.

Smith, L.R., Barton, E.R., 2014. Collagen content does not alter the passive mechanical properties of fibrotic skeletal muscle in mdx mice. Am. J. Physiol. Cell Physiol. 306 (10), C889–C898.

Stephenson, D.G., Williams, D.A., 1985. Temperature-dependent calcium sensitivity changes in skinned muscle fibres of rat and toad. J. Physiol. 360 (1), 1–12.

Stienen, G.J., Kiers, J.L., Bottinelli, R., Reggiani, C., 1996. Myofibrillar ATPase activity in skinned human skeletal muscle fibres: fibre type and temperature dependence. J. Physiol. 493 (Pt 2), 299–307.

ter Keurs, H.E., Iwazumi, T., Pollack, G.H., 1978. The sarcomere length-tension relation in skeletal muscle. J. Gen. Physiol. 72 (4), 565–592.

Wang, G., Kawai, M., 2001. Effect of temperature on elementary steps of the cross-bridge cycle in rabbit soleus slow-twitch muscle fibres. J. Physiol. 531 (Pt 1), 219–234.

Wood, L.K., Kayupov, E., Gumucio, J.P., Mendias, C.L., Claflin, D.R., Brooks, S.V., 2014. Intrinsic stiffness of extracellular matrix increases with age in skeletal muscles of mice. J. Appl. Physiol. 117 (4), 363–369.

Zhao, Y., Kawai, M., 1994. Kinetic and thermodynamic studies of the cross-bridge cycle in rabbit psoas muscle fibers. Biophys. J. 67 (4), 1655–1668.